

# Simulations of the Irradiation and Temperature Dependence of the Efficiency of Tandem Photoelectrochemical Water-splitting Systems

Sophia Haussener<sup>1</sup>, Shu Hu<sup>2</sup>, Chengxiang Xiang<sup>2</sup>  
Adam Z. Weber<sup>3</sup>, and Nathan S. Lewis<sup>2</sup>

<sup>1</sup>Institute of Mechanical Engineering  
École Polytechnique Fédérale de Lausanne, 1015 Lausanne, Switzerland

<sup>2</sup>Joint Center for Artificial Photosynthesis  
California Institute of Technology, Pasadena, CA 91125, USA

<sup>3</sup>Joint Center for Artificial Photosynthesis  
Lawrence Berkeley National Laboratory, Berkeley, CA 94720, USA

The efficiency of an operating photoelectrochemical solar-fuels-generator system is determined by the system design, the properties and morphology of the system's components, and the operational conditions. We used a previously developed model comprising of i) the detailed balance limit to describe the current-potential performance of the photoabsorber component, and ii) the detailed multi-physics device model solving for the governing conservation equations (mass, momentum, species and charge) spatially resolved in the device, to quantify the performance of photoelectrochemical devices. We investigated the performance and its variations as a function of operational conditions, i.e. daily and seasonal irradiation variations, concentration factor of irradiation, and isothermal device temperature. Additionally, the difference in performance of an integrated photoelectrochemical system and a photovoltaic array connected electrically to a stand-alone electrolyzer system was quantified.

## Introduction

An operational solar-driven electrochemical-fuel-generating reactor that electrolyzes water or that reduces CO<sub>2</sub> involves light absorbers, charge generators, and electrocatalytic components embedded in or connected to conducting phases, whilst insuring product separation for efficiency and safety purposes. All of these components are closely coupled, and their individual performance greatly influences the performance of the integrated generator as a system (1-4). A comprehensive model that includes the detailed device architecture and accounts for the spatially resolved governing physics is therefore required to evaluate quantitatively the overall efficiency of such a system as a function of the design, component properties and morphologies, and operational conditions. Equivalent circuit models have been developed to support component choices of a device, such as the choice of light absorber combinations or electrocatalysts (5-8). Recently, models that solve for the governing coupled conservation equations have been developed in 1D (9), 2D (10, 11), and 3D (12), allowing for a better understanding of the interactions between the properties of the components and the design choices of the system.

This work is a summary of the previously published detailed study on the simulation of the efficiency of a photoelectrochemical device as a function of operating conditions, design, and component properties (11). We used the advanced multi-physics model comprising of an analytical model for the semiconducting light absorbers (detailed balance limit (13)) in combination with a spatially resolved multi-physics device model that solved for the governing conservation equations in the various other parts of the system (10, 11).

## Theoretical

### Governing Equations

Multi-physics Model and Boundary Conditions. The engineering multi-physics PEC model has been described previously (10, 11). The model solves for charge transport and conservation in the liquid electrolyte phase as well as in the solid conducting phases, i.e. the semiconductor, catalyst, and/or transparent conducting oxide (TCO), if present. The electrochemical reactions were assumed to be the electrolysis of water in an acidic environment via the anodic oxygen-evolution reaction (OER), eq. [1], and the cathodic hydrogen-evolution reaction (HER), eq. [2].



The kinetics of the electrochemical water-splitting reaction were modeled by use of Butler-Volmer expressions for the OER and HER, respectively (14). Species transport was given by an advection/diffusion equation, whereas transport for charged species was given by the Nernst-Planck equation (14, 15). The mass and momentum conservation equations were solved to calculate the pressure and velocity vector fields (16, 17). The model also incorporated recent extensions that provide a more complete description of the semiconductor parts of the system, including specifically the detailed balance limit (13), and semi-empirical adaptations thereof. The system was assumed to operate at isothermal conditions.

The boundary condition for the light-absorber tandem cell was given by the solar irradiation, i.e. by the intensity and spectral distribution of the incident photon flux. The boundary conditions for the current conservation equations were given by the performance of the dual-absorber tandem cell, with the cathode-side electrode assumed to be grounded. A best case boundary conditions for species conservation was used, i.e. saturation concentrations of  $\text{O}_2$  and  $\text{H}_2$  were assumed in the anolyte and catholyte chambers, resulting in the absence of concentration gradients of the species. The permeability of the polymeric separators was assumed to be sufficiently low to withstand the pressure differentials expected in the system during operation, hence convective flows were neglected. Matlab was used to calculate the characteristics of the dual-absorber tandem cell, with the output of the Matlab code coupled to a commercial finite-element solver, Comsol Multiphysics, to solve the coupled conservation equations with the previously described boundary conditions.

Semiconductor Physics. The detailed balance limit (13) describes the amount of incident solar irradiation that is absorbed and produces an electron-hole pair, i.e. charge or current, in the semiconductor, minus the current lost due to radiative recombination:

$$i = i_{\text{ph}} - i_{\text{rr}} = q \int_0^{\lambda_g} n_{\text{ph,sol}}(\mathbf{x}, \lambda) d\lambda - q \int_0^{\lambda_g} n_{\text{ph,b}}(\lambda, T) d\lambda. \quad [3]$$

$i_{\text{ph}}$  describes the photocurrent density,  $i_{\text{rr}}$  is the current density lost due to radiative recombination,  $\lambda_g$  is the band-gap energy of the semiconducting light absorber,  $n_{\text{ph,sol}}$  is the spectral photon flux arriving at the earth surface at location  $\mathbf{x}$ , and  $n_{\text{ph,b}}$  is the spectral photon flux due to blackbody radiation at temperature  $T$ . In case of a dual-absorber tandem cell, the irradiation is partially absorbed by the top cell and the remaining above-band-gap radiation,  $\lambda > \lambda_{g,\text{top}}$ , is absorbed by the bottom cell. The resulting performance curve of the dual cell can be approximated by a fitted diode equation of the form

$$i = i_{\text{ph}} - i_0 \left[ \exp\left(\frac{qV + qiR_{\text{ser}}}{kT}\right) - 1 \right] - \frac{V}{R_{\text{sh}}}, \quad [4]$$

where  $i_0$  describes the dark saturation current density and  $R_{\text{ser}}$  and  $R_{\text{sh}}$  are area-normalized series and shunt resistances ( $\Omega \text{ m}^2$ ). For the detailed balance limit, the quantity  $R_{\text{ser}}$  is zero and  $R_{\text{sh}}$  goes to infinity. Non-zero values of  $R_{\text{ser}}$  were additionally used in this study to account semi-empirically for the losses within the semiconductor material.

### Definitions

The instantaneous solar-to-hydrogen (STH) efficiency of a PEC device is defined as

$$\eta = \frac{i \cdot U_{\theta}}{I} \eta_{\text{F}} \eta_{\text{pc}}. \quad [5]$$

$i$  is the current density of the operating device,  $U_{\theta}$  is the equilibrium potential of the electrochemical reaction under the specified conditions, assumed 1.23 V.  $I$  is the solar irradiation ( $\text{W m}^{-2}$ ) at a specific location, date and time, integrated over a 1.5 Air Mass spectral distribution,  $\eta_{\text{F}}$  is the Faradaic efficiency of the electrode reaction, and  $\eta_{\text{pc}}$  is the product collection efficiency, given by eq. [6].  $\eta_{@I=1\text{ kW/m}^2}$  describes the instantaneous efficiency for  $I = 1 \text{ kW m}^{-2}$ . We neglected parasitic reactions at the electrode ( $\eta_{\text{F}} = 1$ ).

$$\eta_{\text{pc}} = \frac{\int_{A_{\text{vc}}} i dA - \int_{A_{\text{sep}}} nFN_{\text{fuel}} dA}{\int_{A_{\text{vc}}} i dA}, \quad [6]$$

i.e. the integrated current over the electrode surface (a: anode, c: cathode) used for the electrochemical reaction minus the product lost due to crossover by diffusion or convection through the chamber-separator surface to the other side of the system. For simplicity we assumed  $\eta_{\text{pc}} = 1$ . The efficiency varies during daytime, the daytime average efficiency is defined by:

$$\bar{\eta}_{\text{d}} = \frac{1}{t_{\text{sunset}} - t_{\text{sunrise}}} \sum_{t=t_{\text{sunrise}}}^{t_{\text{sunset}}} \eta. \quad [7]$$

Similarly, the annual daytime average efficiency is given by:

$$\bar{\eta}_a = \frac{1}{n_{\text{season}}} \sum_{s=1}^{n_{\text{season}}} \bar{\eta}_d. \quad [8]$$

The standard deviation of the annual daytime average efficiency was calculated by:

$$\sigma_a = \sqrt{\frac{1}{n_{\text{season}}(t_{\text{sunset}} - t_{\text{sunrise}}) - 1} \sum_{s=1}^{n_{\text{season}}} \sum_{t_{\text{sunrise}}}^{t_{\text{sunset}}} (\eta - \bar{\eta}_a)^2}. \quad [9]$$

### Model Parameters

The temperature-dependent reference-case materials properties of the various components and the correlations to calculate them are given in table I.

Table I. Correlations and parameters used for the various materials and components in the system, as a function of temperature.

Parameter	Value	Param	Value	Param	Value	Ref.
Correlation: $i_{0,\text{OER/HER}} = i_{0,\text{OER/HER},T_{\text{ref}}} \exp\left(-\frac{E_a}{RT}\right)$						
$i_{\text{R,OER/HER}} = i_{0,\text{OER/HER}} \left[ \left(\frac{c_{\text{red}}}{c_{\text{red},0}}\right)^{\gamma_{\text{red}}} \exp\left(\frac{\alpha_{\text{a,OER/HER}} F \eta_{\text{op}}}{RT}\right) - \left(\frac{c_{\text{ox}}}{c_{\text{ox},0}}\right)^{\gamma_{\text{ox}}} \exp\left(\frac{-\alpha_{\text{c,OER/HER}} F \eta_{\text{op}}}{RT}\right) \right]$						
$i_{0,\text{OER},T_{\text{ref}}}$	4.62 A cm <sup>-2</sup>	$E_{\text{a,OER}}$	48.6 kJ mol <sup>-1</sup>	-	-	(18-20)
$i_{0,\text{HER},T_{\text{ref}}}$	142.02 A cm <sup>-2</sup>	$E_{\text{a,HER}}$	28.9 kJ mol <sup>-1</sup>	-	-	(21, 22)
Correlation: $\kappa_{\text{mem}} = \kappa_{0,\text{mem}} \exp\left(-\frac{E_a}{RT}\right)$						
$\kappa_{0,\text{mem}}$	22.73 S m <sup>-1</sup>	$E_{\text{a,mem}}$	2 kJ mol <sup>-1</sup>	-	-	(23)
Correlation: $\kappa_1 = \kappa_{1,T=293\text{K}} (1 + \alpha [T - 293])$						
$\kappa_{1,T=293\text{K}}$	40 S m <sup>-1</sup>	$\alpha$	0.019 K <sup>-1</sup>	-	-	(24)
Correlation: $\sigma_{\text{TCO}} = \frac{A_0}{R_{s,0} t} \exp\left(-\frac{\Delta E}{kT}\right)$						
$R_{s,0}$	10 Ω/□	$A_0$	3.695	$\Delta E$	0.033 eV	(25)
Correlation: $E_g = E_{g,0} - \frac{\alpha_2 T^2}{T + \beta}$						
$E_{g,0,\text{Si}}$	1.1557 eV	$\alpha_{2,\text{Si}}$	$7.021 \cdot 10^{-4}$ eV K <sup>-1</sup>	$\beta_{\text{Si}}$	1108 K	(26)
$E_{g,0,\text{GaAs}}$	1.5216 eV	$\alpha_{2,\text{GaAs}}$	$8.871 \cdot 10^{-4}$ eV K <sup>-1</sup>	$\beta_{\text{GaAs}}$	572 K	(26)
Correlation: $c_{\text{sat},k} = \exp(A_k + B_k / (T / 100\text{K}) + C_k \ln(T / 100\text{K})) / M_{\text{H}_2\text{O}} \cdot 1000$						
$A_{\text{H}_2}$	-48.1611	$B_{\text{H}_2}$	55.2845	$C_{\text{H}_2}$	16.8893	(27)
$A_{\text{O}_2}$	-66.7354	$B_{\text{O}_2}$	87.4755	$C_{\text{O}_2}$	24.4526	(27)

The decrease in the equilibrium potential for the one-step water-electrolysis reaction with increasing temperature is given by

$$U = U_{\theta} - T \cdot \alpha_3, \quad [10]$$

where  $U_{\theta}$  is the equilibrium potential assuming a hydrogen reference electrode, and  $\alpha_3$  is given by the temperature-dependence of the Gibbs free energy ( $\Delta G = -nFU$ ). The kinetic parameters used in the study are for state-of-the-art catalysts, i.e. Pt-based electrodes for the HER reaction and RuO<sub>2</sub>-based electrodes for the OER reaction (28, 29).

Intermittency and Local Variability of Solar Irradiation. The irradiation intensity of Barstow in Southern California was chosen for the investigations. Barstow has a high solar irradiation and is currently used as a location for large-scale concentrated-solar and photovoltaic power generation. The solar irradiation (with hourly resolution) of Barstow for a typical meteorological spring, summer, autumn and winter day, respectively was obtained from NREL's TMY3 datasets. NREL's 1.5 AM data were used for the spectral radiation distribution, and these spectral data were scaled according to the solar irradiation using the relationship  $I = \int_0^{\infty} n_{\text{ph,sol}}(\mathbf{x}, \lambda) d\lambda$ .

### Device Design

The same basic solar-fuels-generator device designs as in our previous study were investigated herein (10, 11). The results presented herein focus on one of the designs, i.e. the design consists of one planar dual-absorber tandem cell or catalyst-covered dual-junction photovoltaic cell immersed in an electrolyte-filled channel but separated from each other by an impermeable, ion-conducting separator. A conductive layer was added on top of the absorber, photovoltaic device, or electrode, to model properly the conducting light absorber or conducting catalyst layer, or a transparent conductive oxide (TCO) layer protecting against the acidic or alkaline environment. For all designs, no potential loss was assumed in the conducting connection for electron transport between the two electrodes. Each design was characterized by an electrode length ( $l_{\text{el}}$ ), an electrolyte height of thickness ( $t_e$ ), and a separator of thickness ( $t_s$ ), and a ratio of the electrode length to the device length ( $f = l_{\text{el}}/l_d$ ). Unless stated otherwise,  $t_s = 10 \mu\text{m}$  and  $f = 0.9$  were used in the calculations.

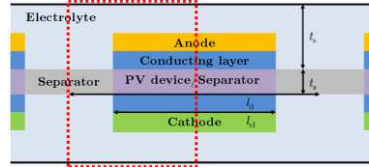


Figure 1. Schematic of the top-to-bottom design used as model device, indicating the various dimensional variables. The red dotted box indicates the modeled unit cells.

## Results

The detailed balance limit for modeling the performance of a dual-absorber tandem cell was used in the first part of the results. Results for a Si/GaAs system (with band gaps of 1.12 eV and 1.43 eV), which is not a current-matched dual absorber tandem-cell, but which has well-known temperature-dependent materials properties, are discussed. The results are then expanded to more realist, measured photoabsorber performances.

## Daily and Annual Variations in Efficiency

Figure 2 depicts the model results for the hourly variation in instantaneous efficiency for four characteristic days of the year. Almost no change in instantaneous efficiency either hourly or for various days in a year was observed when the selected system dimensions resulted in small ohmic electrolyte losses, i.e. at small  $l_{el}$  and large  $t_e$  values.

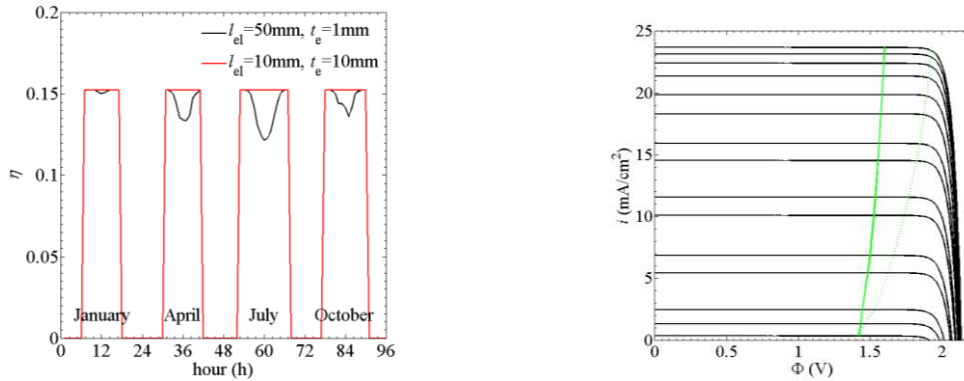


Figure 2. (a) Efficiency variations of the device for four typical seasonal days for Si/GaAs multi-junction cell. (b) The i-V-performance (solid black lines) of the Si/GaAs cell for every hour during the July day (15 hours between 5am and 8pm) and the load curve for  $l_{el} = 50$  mm and  $t_e = 1$  mm (green dotted) and for  $l_{el} = 10$  mm and  $t_e = 10$  mm (green solid), respectively.

For optimized design dimensions (e.g. with  $l_{el} = 10$  mm and  $t_e = 10$  mm),  $\bar{\eta}_d$  and  $\bar{\eta}_a$  were both 15.3%. The instantaneous efficiency was lowest during the hours of the day that had the highest solar irradiation. Similarly, the lowest  $\bar{\eta}_d$  were observed for the days that had the largest solar irradiation. For  $l_{el} = 50$  mm and  $t_e = 1$  mm,  $\bar{\eta}_a$  was 14.6%, with  $\bar{\eta}_d = 15.2, 14.5, 14.1, 14.8\%$  for a typical winter, spring, summer and autumn day, respectively.

## Effect of System Operating Temperature

A variation in the isothermal system temperature is expected to produce two competing changes in the system performance characteristics: a reduction in the absorber efficiency due to increased radiation losses, and an enhancement in the transport and kinetics, leading to less efficiency losses associated with these features of the system. The modeling results demonstrated that the specific integrated solar fuels generator system evaluated exhibited a net decrease in maximal efficiency with increasing temperature, due to the reduction in photovoltage with increasing temperature more than offsetting the reduction in losses produced by the increased electrode kinetics and increased electrolyte conductivity at higher temperatures. For example, for  $l_{el} = 50$  mm, and  $t_e = 1$  mm, when the temperature increased from 300 to 353 K,  $\bar{\eta}_a$  decreased from 14.6% to 13.6% and  $\sigma_a$  decreased from 0.90% to 0.49%. When the temperature was increased, the efficiency variations during a given day decreased, but the system exhibited lower efficiencies at the beginning and end of each day, i.e. exhibited less steep (i.e. less rapid) ramp-up and ramp-down phases in response to sunrise or sunset, respectively.

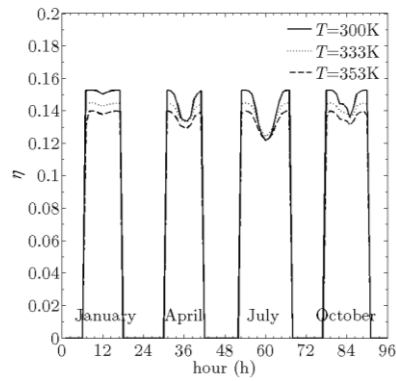


Figure 3.  $\eta$  of a PEC device for four typical seasonal days at three isothermal conditions ( $T = 300, 333, 353$  K), for the Si/GaAs dual-absorber tandem cells,  $l_{el} = 50$  mm,  $t_e = 1$  mm.

### Integrated System Versus Conventional Photovoltaic Module/electrolyzer System

$\eta$ ,  $\bar{\eta}_d$ ,  $\bar{\eta}_a$ ,  $\sigma_a$ , and the yearly amount of fuel produced by an integrated solar fuels generator system were compared to the behavior of a system instead comprised of a conventional photovoltaic (PV) module-based stand-alone system coupled electrically to a stand-alone electrolysis unit. The efficiency of the system comprised of the discrete components can be described as

$$\eta_{PV/electrolyzer} = \eta_{PV} \eta_{DC-DC-converter} \eta_{electrolyzer} \quad [11]$$

where  $\eta_{PV}$  is the energy-conversion efficiency of the PV-based system,  $\eta_{DC-DC-converter}$  is the efficiency of a DC-DC-converter, and  $\eta_{electrolyzer}$  is the efficiency of the electrolyzer, measured by dividing the electrical energy input into the electrolyzer into the value of the free energy of the  $H_2(g)$  produced by the electrolyzer. An electrolyzer efficiency of 75% and a DC-DC-converter efficiency of 85% were used in the calculations.

Figure 4 shows the performance of the stand-alone PV system (Si/GaAs) in combination with the stand-alone electrolyzer system. Si/GaAs does not represent the maximum achievable efficiency of a tandem-cell PV but was chosen to facilitate a straightforward comparison. The stand-alone PV plus stand-alone electrolyzer system displayed its highest  $\eta$  during mid-day and its highest  $\bar{\eta}_d$  at mid-year. Increases in the temperature from 300 K to 353 K of the light absorber components of the discrete system decreased  $\bar{\eta}_a$  of the stand-alone system combination from 13.3% to 10.6%, with a slight increase in  $\sigma_a$  (from 0.53% to 0.57%). The mass of  $H_2$  produced annually,  $m_{tot,H_2,T_0}$ , was 7.5, 7.9, and 8.6  $kg\ m^{-2}\ year^{-1}$  for the stand-alone PV and stand-alone electrolyzer combination, integrated system, and optimized integrated system, respectively at an absorber operating temperature of 300 K in all cases. Hence for these designs, a stand-alone PV and stand-alone electrolyzer combination system would require 13% more area for the production of the same mass of hydrogen per year compared to an integrated system with small total overpotential at  $T = 300$  K. At higher temperatures, the stand-alone system combination exhibited a larger decrease in  $H_2(g)$  production than did the integrated system, requiring 23% more area for the same production of hydrogen per year.

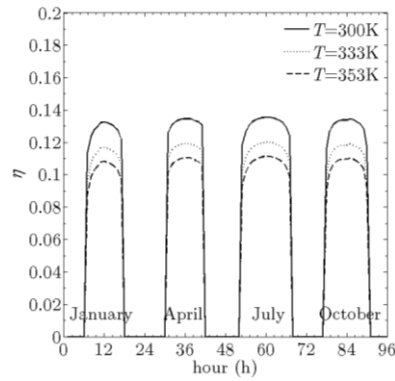


Figure 4.  $\eta$  of a conventional stand-alone PV system with a Si/GaAs dual absorber tandem-cell, electrically connected to a stand-alone electrolyzer, for four typical seasonal days at three isothermal conditions ( $T = 300, 333, 353$  K).

### Efficiency Calculated based on Experimentally Measured Single Absorber Cells

The measured performance data for single-absorber cells made of GaAs and Si, as detailed in Table II, have been used to assess the performance of systems that are constructed using more realistic, currently available, single solar-absorber cells.

Table II. Measured short-current density, open-circuit voltage, fill factor, and temperature coefficients of commercial GaAs (Alta devices<sup>\*</sup>) or Si (Schott<sup>†</sup>(30')) solar cells.

	GaAs cell	Si cell
$i_{sc,0}$	24.39 mA cm <sup>-2</sup>	42.7 mA cm <sup>-2</sup>
$V_{oc,0}$	1.09 V	0.706 V
FF	0.842	0.828
$\alpha_{abs}$	0.084 % K <sup>-1</sup>	0.03 % K <sup>-1</sup>
$\gamma_{abs}$ or $\beta_{abs}$	0.187 % K <sup>-1</sup>	2 mV K <sup>-1</sup>

The intensity dependence and temperature dependence of the performance can be approximated as:

$$i_{sc} = i_{sc,0} (1 + \alpha_{abs} [T - 298]) \cdot I/I_0, \quad [12]$$

$$V_{sc} = V_{sc,0} (1 + \gamma_{abs} [T - 298]), \quad [13]$$

$$V_{oc} = V_{oc,0} - \beta_{abs} (T - 298). \quad [14]$$

The performance of the tandem configuration was calculated by using the Si and GaAs cells in series. The resulting performance of the integrated system and a stand-alone tandem PV plus stand-alone electrolyzer system (electrolyzer efficiency of 75% and a DC-DC-converter efficiency of 85%) using Si/GaAs-based dual absorber tandem-cell based on measured single cell performance are depicted in Figure 5.

The realistic stand-alone PV plus stand-alone electrolyzer system displayed its highest  $\eta$  during mid-day and its highest  $\bar{\eta}_d$  at mid-year. Increases in the temperature from 300 K to 353 K of the photoabsorber components of the discrete system decreased

<sup>\*</sup> [www.altadevices.com/pdfs/single\\_cell.pdf](http://www.altadevices.com/pdfs/single_cell.pdf)

<sup>†</sup> [http://www.schott.com/photovoltaic/english/download/schott\\_perform\\_mono\\_255-270\\_3bb\\_new\\_frame\\_data\\_sheet\\_en\\_0312.pdf](http://www.schott.com/photovoltaic/english/download/schott_perform_mono_255-270_3bb_new_frame_data_sheet_en_0312.pdf)

$\bar{\eta}_a$  of the stand-alone system combination from 11.2% to 8.7%, with a slight increase in  $\sigma_a$  (from 0.24% to 0.27%). The integrated system with  $l_{el} = 50$  mm, and  $t_e = 1$  mm, showed  $\bar{\eta}_a = 11.3\%$  and 6.4% for  $T = 300$  K and 353 K, respectively, with slight increase in  $\sigma_a$  (from 0.02% to 0.03%). Changing the dimensions of the system to  $l_{el} = 10$  mm, and  $t_e = 10$  mm resulted in an increase in  $\bar{\eta}_a$  to values of 14.3% and 10.6% for  $T = 300$  K and 353 K, respectively, with decrease in  $\sigma_a$  (from 0.34% to 0.28%). The integrated system only outperformed the stand-alone PV system coupled electrically to a stand-alone electrolysis unit when the integrated system was designed to have a significantly reduced overpotential. The annually produced hydrogen mass decreased from 7.5, 7.9, and 8.6  $\text{kg m}^{-2} \text{ year}^{-1}$  to 6.5, 5.9, 8.3  $\text{kg m}^{-2} \text{ year}^{-1}$  for the stand alone PV and stand-alone electrolyzer system, the integrated system, and the optimized integrated system, respectively, when using dual absorber tandem-cells that exhibited realistic, measured performance instead of operating at the ideal, detailed-balance performance limits, at  $T = 300$  K.

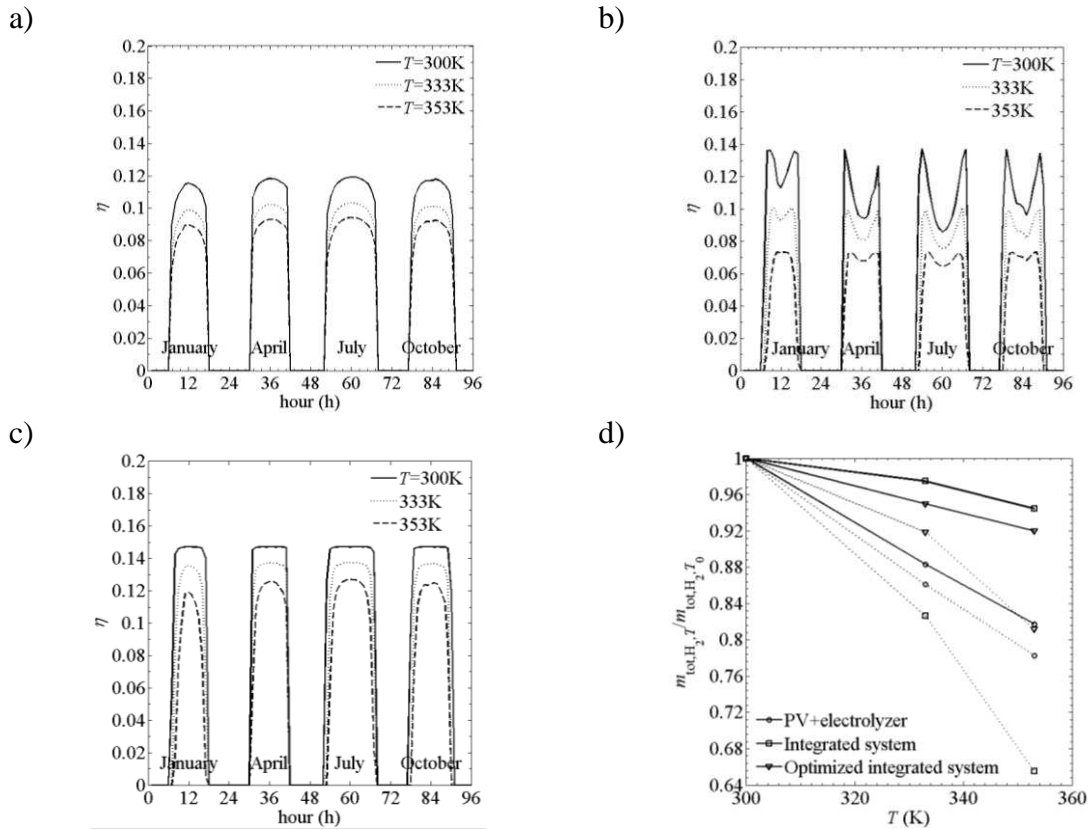


Figure 5. (a)  $\eta$  of PV+electrolyzer system with a Si/GaAs dual absorber tandem structure based on the measured individual cell performance for four typical seasonal days at three isothermal conditions ( $T = 300, 333, 353$  K), and (b,c)  $\eta$  of a PEC device with a Si/GaAs dual absorber tandem-cell based on measured individual cell performance for four typical seasonal days at three isothermal conditions ( $T = 300, 333, 353$  K) for (b)  $l_{el} = 50$  mm, and  $t_e = 1$  mm, and (c)  $l_{el} = 10$  mm, and  $t_e = 10$  mm, and (d) the normalized annually integrated fuel production with  $m_{\text{tot,H}_2,T_0} = 6.6, 5.9,$  and  $8.3 \text{ kg m}^{-2} \text{ year}^{-1}$  for detailed balance limit (solid) and the realistic case (dotted).

## Summary and Conclusion

The largest variation in efficiency during the day and year were observed at the local or global irradiation maxima. These variations in efficiency were especially pronounced for systems that had a relatively large total overpotential, i.e. for devices with a larger electrode length, smaller electrolyte height, lower electrolyte conductivity, and/or smaller band gap combinations of light absorbers. A system designed to produce constant efficiency throughout the year therefore should be designed to operate at maximum efficiency under the maximal solar irradiation at the planned location.

Increased isothermal device temperatures led to a reduction in maximal device efficiency and less steep ramp up and ramp down at the beginning and end of the day, due to decreased performance of the dual-absorber tandem cell with increased temperature. Nevertheless, the midday and midyear variations in efficiency decreased, due to a reduction in the total overpotential, i.e. reduced transport and kinetic losses, with increasing device temperatures. The competition between decreased light absorber performance and increased transport performance with increasing temperature leads to an interesting conclusion, in that a PEC device with a limiting overpotential can gain in annually averaged efficiency if it is not driven at constant lower system temperature but instead is dynamically adapted to higher operating temperatures as the solar irradiation increases, which will occur naturally throughout a day. For a device with low, non-limiting overpotentials, i.e.  $\sigma_a=0$ , the increased transport performance with increased temperature will not lead to additional gains in efficiency and, consequently, such a device will show the best annual performance at low temperatures.

The modeling also allowed for comparison of integrated systems and conventional stand-alone PV plus stand-alone electrolyzer system. The simulations showed that integrated systems can benefit from the small current densities by significantly increasing the “internal electrolyzer efficiency”. A conventional PV plus electrolyzer system (with electrolyzer efficiency of 75% and DC-DC-converter efficiency of 85%) made from exemplary Si and GaAs tandem light absorbers required 13% more area to produce the same annual amount of hydrogen as would be produced by an integrated system with comparable solar absorbers. Additionally, the discrete component PV plus electrolyzer system did not benefit from enhanced kinetics and transport due to enhanced temperatures, additionally enlarging the performance difference, i.e. 23% more area was needed for a discrete component system with the light absorbers at 353 K versus an integrated system at an isothermal operating temperature of  $T = 353$  K.

This work provides a predictive modeling and simulation framework for evaluation of the performance of such systems under varying temperature and irradiation conditions.

## Acknowledgements

We acknowledge the Joint Center for Artificial Photosynthesis, a DOE Energy Innovation Hub, supported through the Office of Science of the U.S. Department of Energy under Award Number DE-SC0004993. We thank Harry Atwater for fruitful discussions on temperature-dependent analysis of realistic systems.

## References

- (1) O. Khaselev and J. A. Turner, *Science*, 1998, **280**, 425–427.
- (2) S. Y. Reece, J. A. Hamel, K. Sung, T. D. Jarvi, A. J. Esswein, J. J. H. Pijpers and D. G. Nocera, *Science*, 2011, **334**, 645–648.
- (3) J. Brillet, J.-H. Yum, M. Cornuz, T. Hisatomi, R. Solarska, J. Augustynski, M. Graetzel and K. Sivula, *Nat Photon*, 2012, **6**, 824–828.
- (4) H. Dotan, O. Kfir, E. Sharlin, O. Blank, M. Gross, I. Dumchin, G. Ankonina and A. Rothschild, *Nat Mater*, 2013, **12**, 158–164.
- (5) M. T. Winkler, C. R. Cox, D. G. Nocera and T. Buonassisi, *Proceedings of the National Academy of Sciences*, 2013, **110**, E1076–E1082.
- (6) R. Rocheleau and E. Miller, *International Journal of Hydrogen Energy*, 1997, **22**, 771–782.
- (7) Y. Surendranath, D. K. Bediako and D. G. Nocera, *Proceedings of the National Academy of Sciences of the United States of America*, 2012, 1–5.
- (8) S. Hu, C. Xiang, S. Haussener, A. D. Berger and N. S. Lewis, *Energy Environ. Sci.*, 2013, in press.
- (9) L. Andrade, T. Lopes, H. A. Ribeiro and A. Mendes, *International Journal of Hydrogen Energy*, 2011, **36**, 175 – 188.
- (10) S. Haussener, C. Xiang, J. M. Spurgeon, S. Ardo, N. S. Lewis and A. Z. Weber, *Energy Environ. Sci.*, 2012, **5**, 9922 – 9935.
- (11) S. Haussener, S. Hu, C. Xiang, A. Z. Weber and Lewis, *Energy Environ. Sci.*, 2013, in press.
- (12) C. Carver, Z. Ulissi, C. Ong, S. Dennison, G. Kelsall and K. Hellgardt, *International Journal of Hydrogen Energy*, 2012, **37**, 2911 – 2923.
- (13) W. Shockley and H. J. Queisser, *Journal of Applied Physics*, 1961, **32**, 510–519.
- (14) A. J. Bard and L. R. Faulkner, *Electrochemical methods - Fundamentals and applications*, John Wiley & Sons: New York, 2nd edn., 2000.
- (15) J. Newman and K. Thomas-Alyea, *Electrochemical systems*, John Wiley & Sons, 2004.
- (16) S. Patankar, *Numerical heat transfer and fluid flow*, McGraw-Hill Inc., US, 1980.
- (17) J. H. Ferziger and M. Peric, *Computational methods for fluid dynamics*, Springer-Verlag, 2001.
- (18) K. Kinoshita, *Electrochemical Oxygen Technology*, John Wiley and Sons, Inc., 1992.
- (19) L. Krikunov, L. Bunakova, S. Zabusova and L. Krishtalik, *Electrochimica Acta*, 1994, **39**, 137 – 142.
- (20) A. Damjanovic, A. Dey and J. O. Bockris, *Journal of The Electrochemical Society*, 1966, **113**, 739–746.
- (21) N. M. Markovic, B. N. Grgur and P. N. Ross, *The Journal of Physical Chemistry B*, 1997, **101**, 5405–5413.
- (22) W. Sheng, H. A. Gasteiger and Y. Shao-Horn, *Journal of The Electrochemical Society*, 2010, **157**, B1529–B1536.
- (23) H. Ito, T. Maeda, A. Nakano and H. Takenaka, *International Journal of Hydrogen Energy*, 2011, **36**, 10527 – 10540.
- (24) H. E. Darling, *Journal of Chemical & Engineering Data*, 1964, **9**, 421–426.
- (25) J. George and C. Menon, *Surface and Coatings Technology*, 2000, **132**, 45 – 48.
- (26) P. Singh and N. Ravindra, *Solar Energy Materials and Solar Cells*, 2012, **101**, 36 – 45.
- (27) W. Haynes, *CRC Handbook of Chemistry and Physics*, Taylor & Francis, 2011.
- (28) J. O. M. Bockris, I. A. Ammar and A. K. M. S. Huq, *The Journal of Physical Chemistry*, 1957, **61**, 879–886.
- (29) G. Lodi, E. Sivieri, A. Battisti and S. Trasatti, *Journal of Applied Electrochemistry*, 1978, **8**, 135–143.
- (30) M. A. Green, K. Emery, Y. Hishikawa, W. Warta and E. D. Dunlop, *Progress in Photovoltaics: Research and Applications*, 2013, **21**, 1–11.